

UC San Diego

UC San Diego Previously Published Works

Title

NiFe Nanoparticle Nest Supported on Graphene as Electrocatalyst for Highly Efficient Oxygen Evolution Reaction

Permalink

<https://escholarship.org/uc/item/5q98c167>

Authors

Lyu, Zhaoyuan

Yu, Sheng

Wang, Maoyu

et al.

Publication Date

2023-11-01

DOI

10.1002/sml.202308278

Peer reviewed

# NiFe Nanoparticle Nest Supported on Graphene as Electrocatalyst for Highly Efficient Oxygen Evolution Reaction

Zhaoyuan Lyu, Sheng Yu, Maoyu Wang, Peter Tieu, Jiachi Zhou, Qiurong Shi, Dan Du, Zhenxing Feng, Xiaoqing Pan, Hongfei Lin, Shichao Ding,\* Qiang Zhang,\* and Yuehe Lin\*

Designing cost-effective electrocatalysts for the oxygen evolution reaction (OER) holds significant importance in the progression of clean energy generation and efficient energy storage technologies, such as water splitting and rechargeable metal–air batteries. In this work, an OER electrocatalyst is developed using Ni and Fe precursors in combination with different proportions of graphene oxide. The catalyst synthesis involved a rapid reduction process, facilitated by adding sodium borohydride, which successfully formed NiFe nanoparticle nests on graphene support (NiFe NNG). The incorporation of graphene support enhances the catalytic activity, electron transferability, and electrical conductivity of the NiFe-based catalyst. The NiFe NNG catalyst exhibits outstanding performance, characterized by a low overpotential of 292.3 mV and a Tafel slope of 48 mV dec<sup>-1</sup>, achieved at a current density of 10 mA cm<sup>-2</sup>. Moreover, the catalyst exhibits remarkable stability over extended durations. The OER performance of NiFe NNG is on par with that of commercial IrO<sub>2</sub> in alkaline media. Such superb OER catalytic performance can be attributed to the synergistic effect between the NiFe nanoparticle nests and graphene, which arises from their large surface area and outstanding intrinsic catalytic activity. The excellent electrochemical properties of NiFe NNG hold great promise for further applications in energy storage and conversion devices.

## 1. Introduction

Given the rapid pace of energy consumption and severe environmental pollution caused by traditional fossil fuels, developing clean and renewable energy technologies has become a compelling necessity. To meet the growing market and development requirements, the oxygen evolution reaction (OER), in water electrolysis, has aroused enthusiastic attention. It has been proposed to address some challenges of sustainable energy devices and technologies.<sup>[1–4]</sup> One of the main obstacles in water splitting is the sluggish multistep reaction pathway of water oxidation, which requires a high-energy input.<sup>[5–7]</sup> Hence, developing stable, highly active, and cost-effective water oxidation catalysts is essential for the widespread application of these processes in energy production.<sup>[8]</sup> Currently, noble-metal catalysts like IrO<sub>2</sub> and RuO<sub>2</sub> are considered the most reliable commercial materials and are widely

Z. Lyu, Q. Shi, D. Du, S. Ding, Q. Zhang, Y. Lin  
School of Mechanical and Materials Engineering  
Washington State University  
Pullman, WA 99164, USA  
E-mail: s5ding@ucsd.edu; q.zhang@wsu.edu; yuehe.lin@wsu.edu

S. Yu, Q. Zhang  
Department of Chemistry  
Washington State University  
Pullman, WA 99164, USA


M. Wang, Z. Feng  
School of Chemical, Biological, and Environmental Engineering  
Oregon State University  
Corvallis, OR 97331, USA

P. Tieu  
Department of Chemistry  
University of California Irvine  
Irvine, CA 92697, USA

J. Zhou, S. Ding  
Department of Nanoengineering  
University of California San Diego  
La Jolla, CA 92093, USA

X. Pan  
Irvine Materials Research Institute (IMRI)  
Department of Physics and Astronomy  
Department of Materials Science and Engineering  
University of California Irvine  
Irvine, CA 92697, USA

H. Lin  
The Gene and Linda Voiland School of Chemical Engineering and  
Bioengineering  
Washington State University  
Pullman, WA 99164, USA

 The ORCID identification number(s) for the author(s) of this article can be found under <https://doi.org/10.1002/smll.202308278>

© 2023 The Authors. Small published by Wiley-VCH GmbH. This is an open access article under the terms of the Creative Commons Attribution License, which permits use, distribution and reproduction in any medium, provided the original work is properly cited.

DOI: 10.1002/smll.202308278

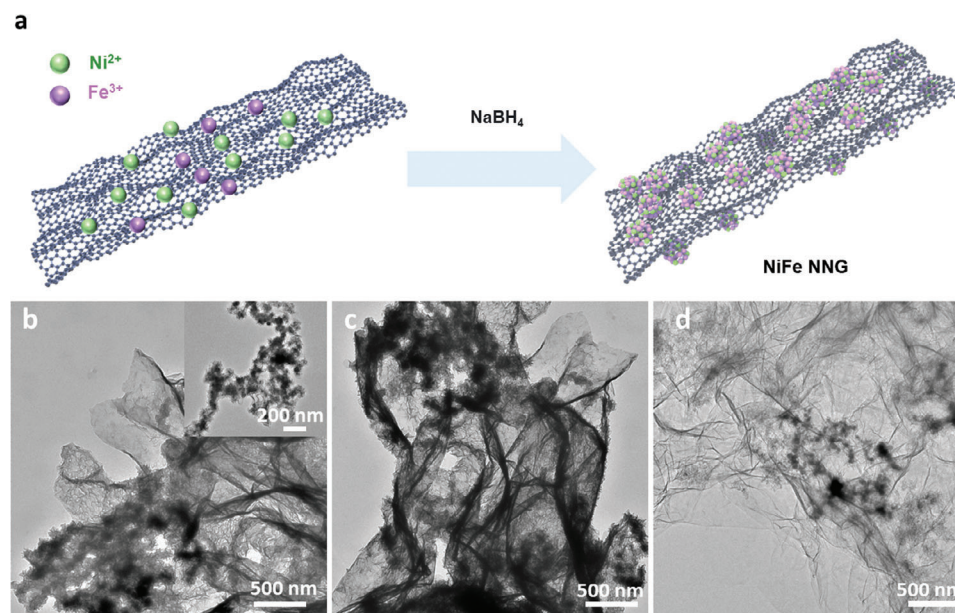


**Figure 1.** a) Schematic illustration of the synthesis of NiFe NNG. b–d) TEM images of NiFe NNG-10, NiFe NNG-20, and NiFe NNG-30, respectively. Inset in b: isolated NiFe nanoparticles.

regarded as the benchmark catalysts for OER.<sup>[9,10]</sup> Despite their excellent properties in OER catalysis, the prohibitive cost of these precious metals restricts their extensive applications in various fields.

Extensive research has been conducted to discover alternative non-noble metal catalysts that can match the performance of noble metal catalysts, yet are made of low-cost, earth-abundant materials.<sup>[11–14]</sup> Transition metal-based catalysts, such as iron and nickel, are treated as competent candidates due to their low overpotential and excellent stability in alkaline conditions.<sup>[15–25]</sup> For example, Hao et al. prepared the nanoporous Ni-based solid solution electrode which mimics naturally-formed materials, exhibiting outstanding long-term stability in a wide range of current densities.<sup>[26]</sup> Up to now, some strategies have been used to design NiFe-based electrocatalysts for high-efficiency OER, including three-dimensional (3D) sandwiched NiFe/C arrays on Ni foam;<sup>[27]</sup> directly pyrolyzed Ni/Fe polyphthalocyanine into N-rich Ni–Fe/C;<sup>[28]</sup> and so on.<sup>[29–31]</sup> Our group also synthesized several 3D porous NiFe nanofoams without using any hard or soft template and found that such ultrafine and highly disordered NiFe-based catalysts exhibit outstanding electrocatalytic performance toward OER in alkaline conditions.<sup>[32]</sup> Additionally, researchers have reported that using thinner carbon layer materials can improve the electron transfer from the metals to the carbon, thus enhancing the catalytic activity.<sup>[33]</sup> Especially, graphene-based materials have been extensively studied as electrode materials and catalyst supports because of their high electrical conductivity, large specific surface area, and excellent electron transfer rate on the electrodes.<sup>[29–31,34]</sup> We believe that NiFe catalysts integrating graphene sheets as catalytic composites are expected to have high OER performances and enhance electron transferability and electrical conductivity.<sup>[35]</sup> Although several studies have investigated NiFe–C catalysts, fast anchoring the disordered NiFe nanoparticle on graphene is still unexplored.

This work presents a fast and straightforward method to synthesize bimetallic nanoparticles-graphene composites with an enriched two-dimensional (2D) catalytic interface structure, composed of NiFe nanoparticle nest coupled with different amounts of graphene (NiFe NNG). Specifically, the NiFe NNG is synthesized by adding graphene oxides into mixed Ni and Fe precursors, which are rapidly reduced by sodium borohydride. Due to the outstanding intrinsic catalytic activity of NiFe and the special properties of the graphene, the obtained NiFe NNG exhibits excellent water-splitting OER activities in alkaline media, showing a low overpotential of 292.3 mV at a current density of 10 mA cm<sup>-2</sup>, as well as a small Tafel slope of 48 mV dec<sup>-1</sup>. X-ray absorption spectroscopy (XAS) has been conducted thoroughly on the best-performing electrocatalyst before and after OER tests to analyze the changes in structure and oxidation states.

## 2. Results and Discussion

**Figure 1a** depicts the schematic illustration of the synthesis process for NiFe NNGs. In detail, graphene oxide (GO) is dispersed in water with the assistance of sonication. Then, the Ni and Fe precursors (Ni(NO<sub>3</sub>)<sub>2</sub>·6H<sub>2</sub>O and Fe(NO<sub>3</sub>)<sub>3</sub>·9H<sub>2</sub>O) in a 2:1 mole ratio are dissolved in the GO-dispersed solution with vigorous stirring for ≈5 min at room temperature. The ratio of Ni and Fe (2:1) selected in the precursor solution is based on our previous research.<sup>[32]</sup> A freshly prepared NaBH<sub>4</sub> solution is then quickly injected into the above mixture. The mixture is stirred for 5 min, and then to collect the black solids. Both metal precursors and GO are simultaneously reduced during the nucleation and growth stage, providing a straightforward strategy to prepare NiFe alloys loaded on reduced graphene. The obtained NiFe NNGs are collected through centrifugation followed by freeze-drying (see the Experimental Section in Supporting Information for more details). To investigate the effect of GO quantity on

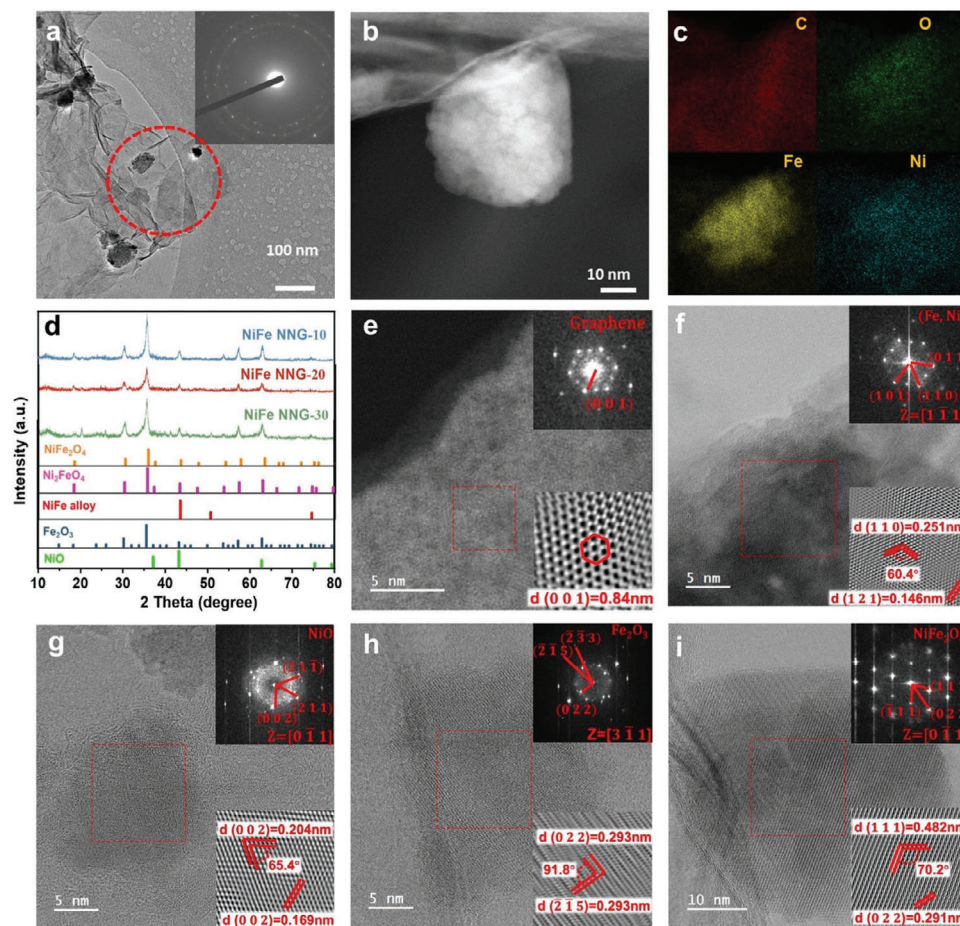


**Figure 2.** a) Low magnification (inset: SAED pattern) and b) high magnification of STEM images of NiFe NNG-20. c) EDS mapping images of C, O, Fe, and Ni, respectively. d) XRD patterns of the NNGs. e–i) TEM images of the as-synthesized NiFe NNG-20. Upper inset: SAED pattern. Below inset: HRTEM crystal lattice images.

the structural and catalytic performance of NiFe NNGs, different amounts of GO (10, 20, and 30 mg) are used. These NNGs are named NiFe NNG-10, NiFe NNG-20, and NiFe NNG-30, respectively. The distribution of NiFe on graphene was investigated using transmission electron microscopy (TEM) in Figure 1b–d. As we can see from the morphology of NiFe NNG, the NiFe nanoparticles are dispersed on the surface of the graphene surface, forming a dense distribution in NiFe NNG-10 and NiFe NNG-20. However, some isolated NiFe nanoparticles not coupled with graphene are also observed (inset of Figure 1b). This occurs because the amount of GO in the precursor is insufficient to accommodate all the reduced Ni and Fe, thus limiting the complete formation of the nest structure. Notably, the NiFe nanoparticles within the NiFe NNG catalyst are composed of a multitude of individual nanoparticles that are intricately assembled together. For the NiFe NNG-30, some bare graphene sheets without NiFe nanoparticles are observed (Figure 1d). Hence, 20 mg of starting GO is determined to be the most suitable amount for anchoring NiFe nanoparticles uniformly on their surface and constructing an electrocatalyst nest structure from a morphology perspective.

The morphology of NiFe NNG-20 was further characterized by scanning TEM (STEM) images (Figure 2a), and we can see

that NiFe nanoparticles are located on the surface of graphene. Additionally, the selected area electron diffraction (SAED) pattern in the inset shows the crystal structure of the as-prepared NiFe nanoparticles. As shown in Figure 2b, the NiFe nanoparticles are anchored to graphene, which constructs the basic unit of the electrocatalyst nest. STEM energy-dispersive X-ray spectroscopy (EDS) elemental mapping further confirms the uniform distribution of Fe and Ni on the hybrids, as shown in Figure 2c and Figure S1 (Supporting Information). Moreover, the cross-sectional compositional linear scan (Figure S2, Supporting Information) further proved that the localized structure in NiFe nanoparticles consisted of Ni and Fe nanoparticles. Powder X-ray diffraction (PXRD) was employed to measure and reveal the crystal structure of NiFe NNG-10, NiFe NNG-20, and NiFe NNG-30. These three composite materials showed similar characteristic peaks (Figure 2d). Specifically, the peaks observed at 43.4°, 50.9°, and 74.5° correspond well with the face-centered cubic structure of Ni–Fe alloy (PDF#47-1417), attributed to its (111), (200), and (220) facets, respectively. Furthermore, the Ni–Fe mixed oxide diffraction pattern showed sharp peaks at the  $2\theta$  values of 18.3°, 25.3°, 30.2°, 30.5°, 43.2°, 57.2°, 62.9°, corresponding to the presence of the Rhombohedral phase crystallographic structure of

$\text{Fe}_2\text{O}_3$  (JCPDS: 39–1346), while the existence of the diffraction peaks at  $2\theta$  values of  $37.2^\circ$ ,  $43.3^\circ$ , and  $63.0^\circ$  are owing to the structure of NiO (JCPDS: 47–1049). The intensive peaks situated at the  $2\theta$  values of  $18.4^\circ$ ,  $30.3^\circ$ ,  $35.6^\circ$ ,  $37.4^\circ$ ,  $43.4^\circ$ ,  $53.8^\circ$ ,  $57.3^\circ$ ,  $63^\circ$ , and  $74.6^\circ$  are ascribed to the face-centered cubic phase crystallographic structure of spinel  $\text{NiFe}_2\text{O}_4$  (JCPDS: PDF#10-0325). Moreover, the existence of the diffraction peaks at  $2\theta$  at  $18.5^\circ$ ,  $30.4^\circ$ ,  $35.9^\circ$ ,  $37.6^\circ$ ,  $43.6^\circ$ ,  $54.1^\circ$ , and  $57.7^\circ$  indicates the face-centered cubic crystallographic structure of  $\text{FeNi}_2\text{O}_4$  (JCPDS: PDF#01-074-6507).<sup>[36,37]</sup> It is also noted that the obvious peak at  $\approx 11^\circ$  (0.84 nm) corresponds to the (001) plane of GO.<sup>[38]</sup> In addition, the microstructures of the NiFe NNG-20 were investigated by bright field STEM (BF-STEM) imaging, as illustrated in Figure 2e–i. Similarly, the information on lattice spacings can be obtained through fast Fourier transformation (FFT) and inverse fast Fourier transformation (IFFT). It is worth noting that graphene lattice fringes ( $d = 0.84$  nm) were also found in the STEM imaging of NiFe NNG-20, which can be attributed to the (001) crystal plane (Figure 2e). Based on the crystal orientation relationship, the lattice spacings of 0.146 and 0.251 nm should be assigned to the NiFe (121) and (110) moieties, respectively, with the corresponding crystallographic zone axis being (111), as illustrated in Figure 2f. This confirms the presence of alloyed NiFe species, which is consistent with the XRD results. Interestingly, in the STEM imaging of NiFe NNG-20, lattice spacings and crystallographic zone axes (Figure 2g–i) that are in agreement with  $\text{Fe}_2\text{O}_3$ , NiO, and  $\text{NiFe}_2\text{O}_4$  are identified. This is highly consistent with the above XRD results, indicating that NiFe NNG-20 consists of NiFe alloy mixed with metal oxides. The oxide compounds might come from oxidation during the freeze-drying and storage process toward NiFe species by air.

To understand the oxidation state and local structures of Ni and Fe in the alloys, X-ray absorption spectroscopy (XAS) measurements were performed.<sup>[39–41]</sup> The X-ray absorption near-edge structure (XANES) spectra show that the absorption edge position of NiFe NNG-20 in the Ni K-edge is higher than that of NiO, indicating that the Ni species in the NNGs have an oxidation state higher than +2 (Figure 3a).<sup>[42]</sup> Besides, the Fe K-edge XANES spectrum of NNG is located between FeO and  $\text{Fe}_2\text{O}_3$  (Figure 3b), suggesting that the average valence state of Fe atoms falls between +2 and +3. The surface composition of NiFe NNG-20 was further analyzed by X-ray photoelectron spectroscopy (XPS) and the presence of Ni, Fe, C, and O elements was revealed (Figure 3c). The results indicated that the atomic ratio of Ni (4.10 at.%) to Fe (9.08 at.%) in the NiFe NNG catalyst is  $\approx 1:2.21$ . This ratio closely aligns with the 1:2.38 ratio obtained from X-ray fluorescence (XRF) analysis, which reported Ni at 29.55% and Fe at 70.45% (refer to Figure S3a). The complex composition of NiFe NNG may form a thermodynamically stable substance unrelated to the starting precursor Ni/Fe molar ratio. It should be noted that B (boron) remains present in the catalyst, and the doping of such a heteroatom enhances its conductivity.<sup>[43]</sup> The high-resolution O1s XPS spectrum (Figure 3d) could be deconvoluted into two peaks centered at 530.6 and 534.8 eV, which could be indexed to Ni–O/Fe–O and C–O–C. Figure 3e shows the high-resolution XPS spectrum of Ni  $2p_{1/2}$  and  $2p_{3/2}$ , which consists of  $\text{Ni}^{2+}$  (855.2 and 872.9 eV) and  $\text{Ni}^{3+}$  (856.9 and 874.7 eV) due to the exposure to air and satellite (862.0 and 880.1 eV) peaks. This is also mutually confirmed with the X-ray absorption near-edge structure

spectrum (XANES) of Ni species.<sup>[44,45]</sup> The high-resolution XPS spectrum of Fe (Figure 3f) also shows the peaks of Fe  $2p_{1/2}$  and  $2p_{3/2}$ , confirming the existence of +2 and +3 valence states of Fe species in NiFe NNG-20, which also proved the existence of mixture species of  $\text{FeNi}_2\text{O}_4$  and  $\text{NiFe}_2\text{O}_4$ .<sup>[46]</sup> Raman spectrum of NiFe NNG-10, NiFe NNG-20 and NiFe NNG-30 (Figure 3g) display the D, G and 2D bands at 1347, 1578, and 2709  $\text{cm}^{-1}$ , respectively, which are characteristic of graphene.<sup>[47,48]</sup> Moreover, the intensity ratio of the two bands ( $I_D/I_G$ ) is related to the quantity of defects and structural imperfections in carbon materials,<sup>[49]</sup> and all of the NiFe NNGs own a higher  $I_D/I_G$  ratio than that of bare GO,<sup>[50]</sup> which means the involved NiFe caused more disordered carbon species. Among the three composites, NiFe NNG-30 exhibits the lowest  $I_D/I_G$  ratio (0.82) because it has the highest graphene content compared to the others. In contrast, NiFe NNG-20 has the highest  $I_D/I_G$ , indicating it possesses the most defects, which can lead to the best electrocatalytic performance. The 3D porous structures of NiFe NNG-10, NiFe NNG-20, and NiFe NNG-30 are demonstrated by nitrogen adsorption and desorption analysis (Figure 3h). This indicates that NiFe NNG-20 possesses the highest specific Brunauer-Emmett-Teller (BET) surface area ( $57.83 \text{ m}^2 \text{ g}^{-1}$ ) among the three electrocatalytic materials. This higher surface area indicates the presence of more catalytic sites, highlighting the potential for enhanced catalytic activity. This phenomenon can be attributed to the higher presence of NiFe nanoparticles directly dispersed on the graphene surface (as depicted in Figure 1c). This distribution of nanoparticles leads to an increased number of defects (as illustrated in Figure 3g), ultimately resulting in a higher specific surface area for NiFe NNG-20. Compared with bare reduced graphene ( $13.66 \text{ m}^2 \text{ g}^{-1}$ , Figure S4, Supporting Information), the increased specific surface area of NiFe NNGs will benefit the OER properties. The pore size distribution indicates the mesoporous nature of all three samples, with pore sizes ranging from micro to mesopores (Figure 3i). Results show that the total pore volume of NiFe NNGs-10/20/30 is 0.0583, 0.1241, and  $0.1486 \text{ cm}^3 \text{ g}^{-1}$ , respectively. This combination of high surface area, a large pore volume, and a higher concentration of defects contribute to the enhanced electrocatalytic performance of NiFe NNG-20 compared to the other two composites.<sup>[44–49,51–54]</sup>

The electrochemical characteristics of NNGs were first investigated using electrochemical impedance spectroscopy (EIS). The charge transfer resistance decreases with the increase of graphene content (Figure S5, Supporting Information), revealing that introducing graphene can enhance electrical conductivity and improve electron transfer during the catalytic process. Figure 4a features the OER polarization curves of both the studied NNGs and  $\text{IrO}_2$  as the reference sample. NiFe NNG-20 exhibits an OER potential ( $E_j = 10$ ) of 1.522 V while maintaining a current density of  $10 \text{ mA cm}^{-2}$ . This OER potential is much better than that of the reference  $\text{IrO}_2$  (1.558 V) and other NNGs (1.534 V for NiFe NNG-10; 1.546 V for NiFe NNG-30). NiFe NNG-20 shows an obviously superior performance with a low overpotential of  $\eta = 292.3 \text{ mV}$  at  $10 \text{ mA cm}^{-2}$ . This low overpotential is also exceptional when compared with other reported NiFe-based OER catalysts (Table S1, Supporting Information). NiFe NNG-20 exhibits the lowest overpotential (350.2 mV) compared to NiFe NNG-10 (363.1 mV), NiFe NNG-30 (370.8 mV), and the reference  $\text{IrO}_2$  (400.1 mV) at

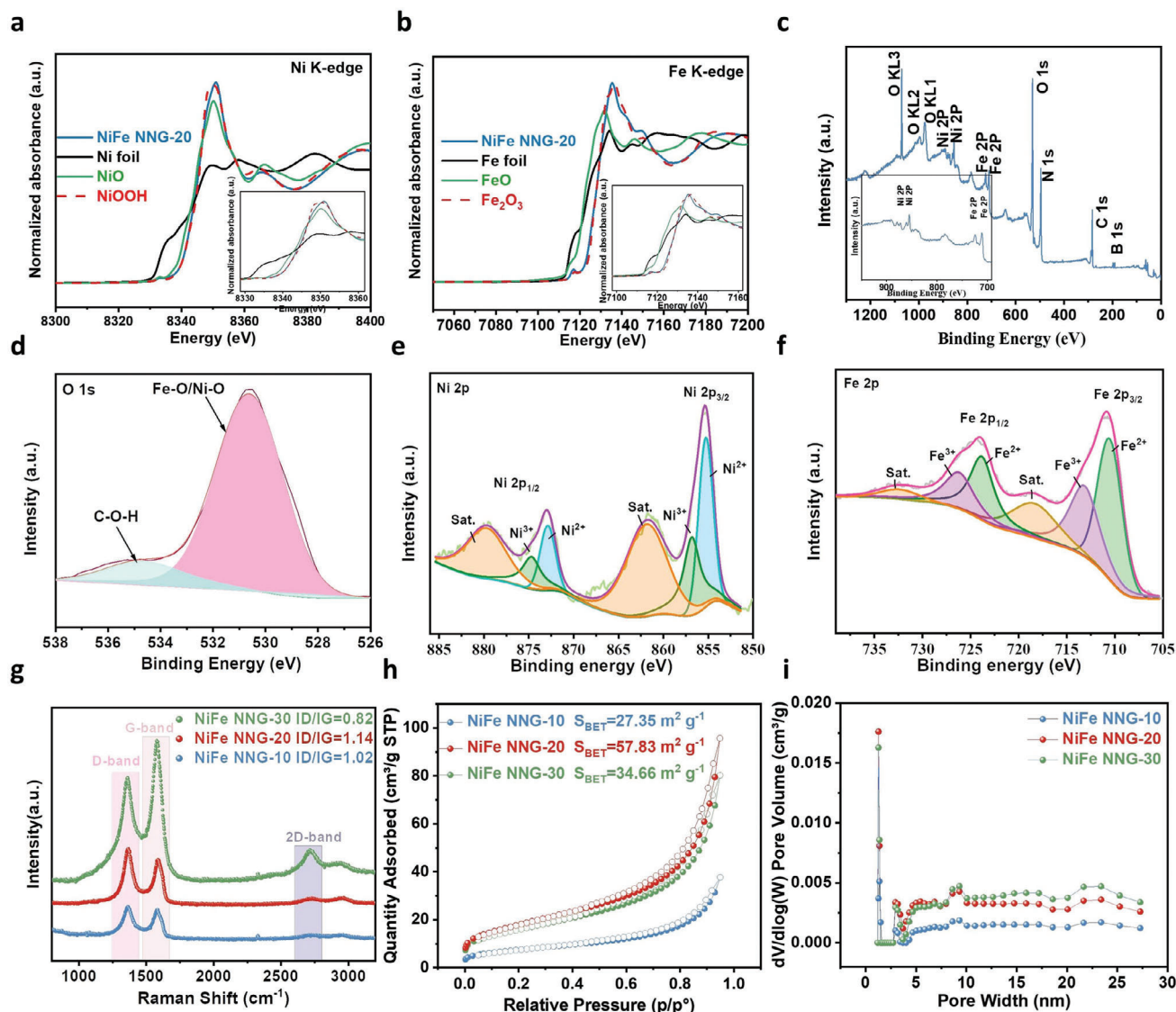


**Figure 3.** a,b) Ni and Fe K-edge XANES spectra of NiFe NNG-20 and reference samples. c) XPS spectrum of NiFe NNG-20. d–f) O 1s, Ni 2p and Fe 2p XPS spectra of NiFe NNG-20. g) Raman spectra of NNGs. h,i)  $N_2$  adsorption-desorption isotherm curves of NiFe NNG-10, NiFe NNG-20, and NiFe NNG-30 by nonlocal density functional theory (NLDFT) method.

50 mA  $cm^{-2}$ . In addition, the Ni NNG-20, Fe NNG-20, and NNG-20 samples display higher overpotentials, indicating that the superior OER performance primarily results from the NiFe (Figure S6, Supporting Information).

Tafel plots shown in Figure 4b depict that the NiFe NNG-20's Tafel slope (48 mV  $dec^{-1}$ ) is slightly smaller than that of commercially available  $IrO_2$  (74 mV  $dec^{-1}$ ) and other reported NNGs, which suggests that OER is kinetically highly favorable on NiFe NNG-20. Electrochemical surface area (ECSA) was determined to exclude the contribution regarding the net amount or surface area. The ECSA can be estimated from the electrochemical double-layer capacitance (Figure S7, Supporting Information).<sup>[55]</sup> The NiFe NNG-20 exhibits the highest ECSA than other NNGs (Figure 4c), demonstrating an increased density of exposed active sites in its structure, which reveals the superiority of NiFe NNG-20 compared to other catalysts in terms of OER perfor-

mance. EIS measurements were conducted at 1.5 V (V vs RHE), and the results are shown in Figure S8 (Supporting Information). The similarity of trends observed in all Nyquist plots indicates that the catalysts' charge transfer processes and electrochemical mechanisms toward OER are comparable. It is noticeable that these catalysts exhibit distinct solution resistances ( $R_s$ ), which can be attributed to the varying contact resistances ( $R_{ct}$ ) between the electrode and the electrolyte.<sup>[56,57]</sup> It can also be observed that NiFe NNG-20 exhibits the lowest  $R_{ct}$  (8.38  $\Omega$ ), further indicating it possesses the lowest charge transfer resistance at the catalyst/electrolyte interface and the fastest electron transfer rate during the OER process.<sup>[58,59]</sup> The current density normalized by ECSA reflects the intrinsic activity of the electrode, and OER activity in the ECSA-normalized LSV (Figure 4d) is also consistent with Figure 4a. The accelerated durability test (ADT) is used to evaluate the stability of NiFe NNG-20. The linear sweep

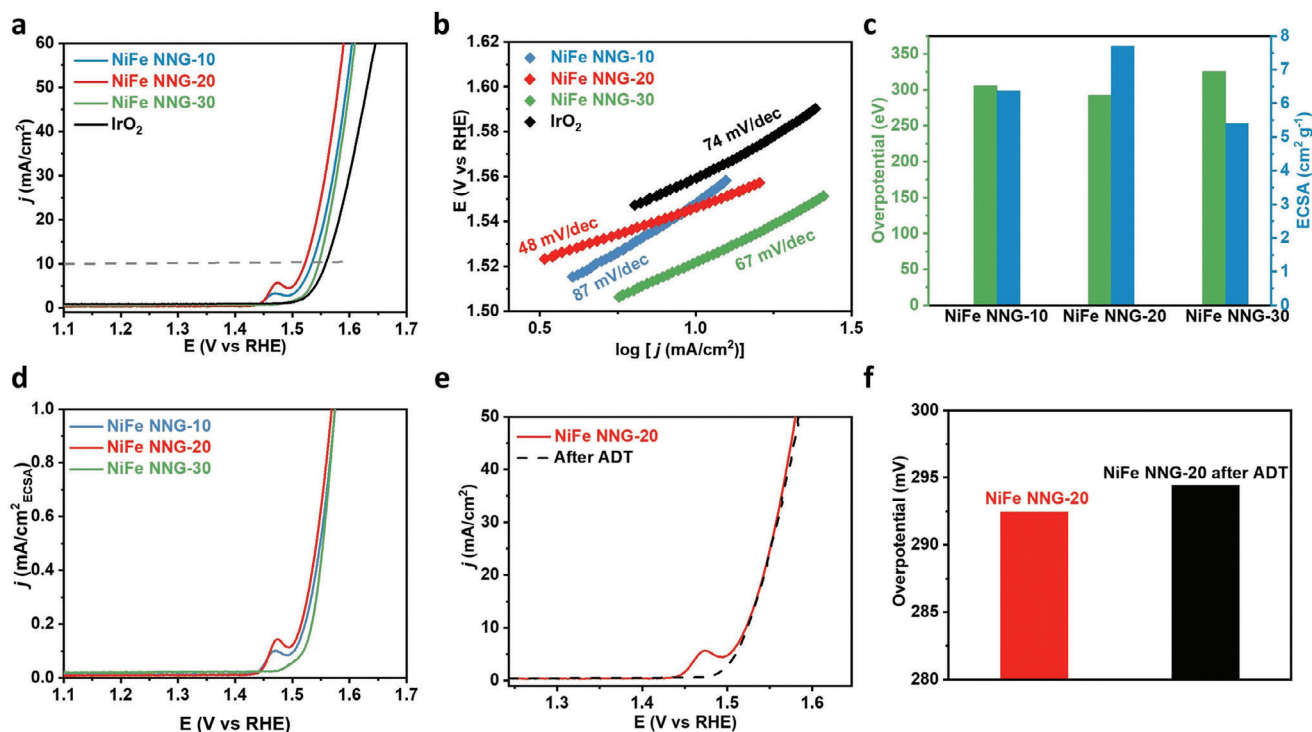


**Figure 4.** a,b) Polarization curves and Tafel plots of NiFe NNG-10, NiFe NNG-20, NiFe NNG-30, and IrO<sub>2</sub>. c) Overpotential and ECSA of NNGs. d) Polarization curves normalized by ECSA for OER. e) LSV curves before and after 2000 potential cycles test in 1 M KOH aqueous solution. f) Overpotential changes after the ADT at a current density of 10 mA cm<sup>-2</sup>.

voltammetry (LSV) curves before and after NiFe NNG-20 endures a 2000 potential cycle test are displayed in Figure 4e. Evidently, the LSV curve of the NiFe NNG-20 after the ADT test shows a slight positive shift of overpotential at 10 mA cm<sup>-2</sup> (Figure 4f). It should be noted that the disappearance of the anodic peak here may be attributed to the catalyst transitioning to an oxidized state. A long-term chronopotentiometric test was also conducted to further evaluate stability, and the results show that NiFe NNG-20 can still maintain 85% of the current response after 20 000 s at 50 mA cm<sup>-2</sup> versus RHE (Figure S9, Supporting Information). The reduced stability might be due to loss of iron. XRF results indicate that, after stability testing, the atomic ratio of Ni to Fe in NiFe NNG-20 is ≈1:1.73, and there is a noticeable decrease in the Fe mass ratio, dropping to 62.79% from 70.45% before the stability testing (Figure S3b, Supporting Information).

To further confirm the evolution of the oxidation state and crystal structure of the constructed NNG, TEM, and XAS measurements were conducted on NiFe NNG-20 at the beginning and end of the OER cycling test. Seldom obvious morphology changes are observed in NiFe NNG-20 after the OER reaction, and the NiFe components still anchor on the graphene (Figure S10, Supporting Information). The XANES of Ni K-edge demonstrates that the oxidation state of Ni increases after OER, which is featured by the increase of white line intensity and right-shifted position (Figure 5a). Similar results were also observed for the Fe element (Figure 5c). The change in the local bonding environment is further investigated by corresponding Fourier transforms (FT) obtained from the extended X-ray absorption fine structure (EXAFS). The Ni/Fe-O peaks shown in the original NiFe NNG-20 are

caused by oxidization in the air, and such results also correspond with XRD and STEM analysis in Figure 2. It can be seen that the intensity of the Ni-Metal backscattering peak, located at 2.1 Å, decreases after the ADT test. This is because the metal/alloy Ni species switch to an oxidation state after a continuous oxidation reaction. Besides, the Ni–O peak of NiFe NNG-20 has become much broader as well as closer to the oxyhydroxide state, which is consistent with the reported mechanism.<sup>[32,60]</sup> Also, for the Fe K-edge FT-EXAFS result (Figure 5d), the Fe–Fe/metal backscattering intensity disappeared after ADT, which further demonstrates the oxidation of the catalyst. These findings suggest that the NiFe NNG-20 electrocatalyst demonstrates both excellent stability and performance in the OER process, with only minor changes in its structure and oxidation states after 2000 potential cycles.

### 3. Conclusion

In conclusion, we have developed a NiFe NNG electrocatalyst to enhance OER catalytic performance under alkaline conditions. We used varying amounts of graphene in the system to construct the NiFe NNG, enabling a comprehensive assessment of their structural properties and catalytic performance. This novel NiFe NNG electrocatalyst can be easily synthesized via a rapid reduction of Ni/Fe/GO precursors. Results indicate that NiFe NNG with 20 mg of graphene (NiFe NNG-20) exhibits superior OER activity compared to those with 10 and 30 mg, as well as the commercial IrO<sub>2</sub> catalyst. Specifically, NiFe NNG-20 achieves a low overpotential of 292.3 mV at a current density of 10 mA cm<sup>-2</sup> and a Tafel slope of 48 mV dec<sup>-1</sup>. The exceptional OER activity

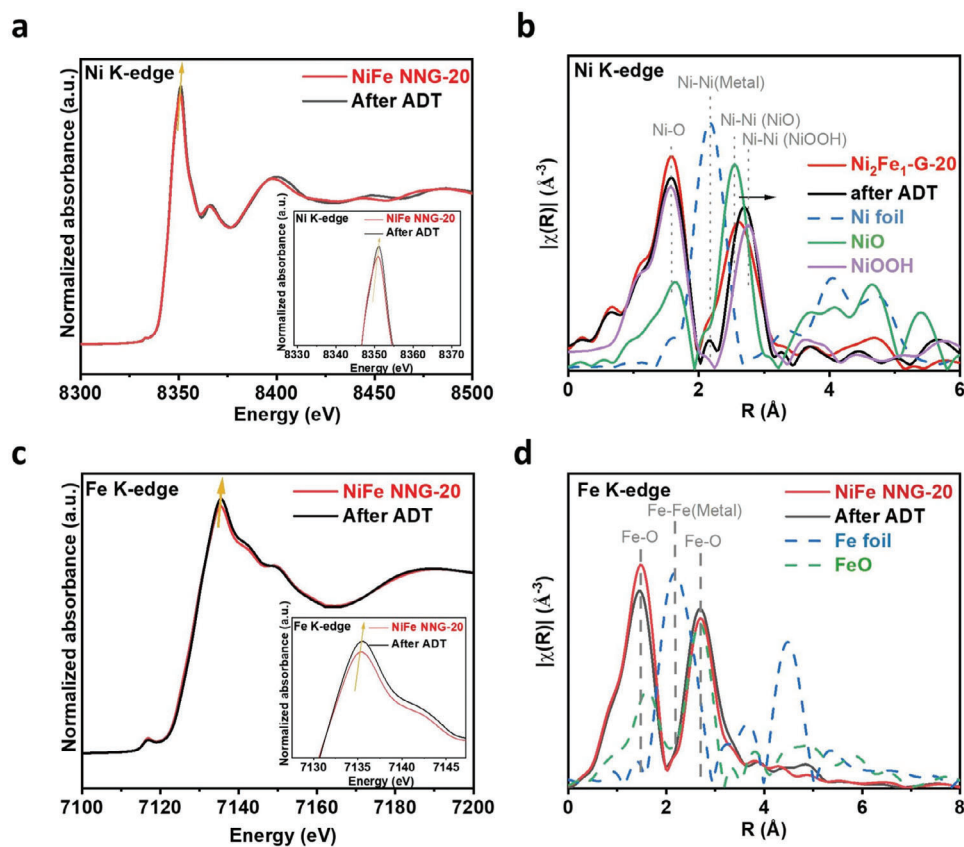


Figure 5. a–d) XANES and EXAFS spectra in Ni K-edge analysis of NiFe NNG-20 before and after ADT.

of NiFe NNG can be ascribed to its large surface area, the outstanding intrinsic catalytic activity of NiFe, and the interactions between NiFe nanomaterials and graphene. These attributes endow the NiFe NNG catalyst with significant potential for applications in future energy storage and conversion devices. The development of such highly efficient and stable electrocatalysts paves the way for enhancing the performance of electrolyzers and other technologies dependent on efficient OER catalysts in alkaline environments.

## Supporting Information

Supporting Information is available from the Wiley Online Library or from the author.

## Acknowledgements

Z.L. and S.Y. contributed equally to this work. The support of NSF grants 1939876 is gratefully acknowledged. QZ would like to thank the support from the WSU start-up fund. This work used resources from the WSU Franceschi Microscopy & Imaging Center for TEM measurements. XAS measurements, supported by the US National Science Foundation (Grant No. CBET-1949870), were done at 20-BM of Advanced Photon Source, a US DOE Office of Science user facility operated for the US DOE by the Argonne National Laboratory, which is supported by DOE under Grant No. DE-AC02-06CH11357. The authors thank all the experimental assistance from Linan Zhu.

## Conflict of Interest

The authors declare no conflict of interest.

## Data Availability Statement

The data that support the findings of this study are available from the corresponding author upon reasonable request.

## Keywords

electrocatalyst, graphene, nanoparticle, NiFe, oxygen evolution

Received: September 20, 2023

Revised: October 31, 2023

Published online:

- [1] D. Li, E. J. Park, W. Zhu, Q. Shi, Y. Zhou, H. Tian, Y. Lin, A. Serov, B. Zulevi, E. D. Baca, C. Fujimoto, H. T. Chung, Y. S. Kim, *Nat. Energy* **2020**, *5*, 378.
- [2] C. Zhu, Q. Shi, S. Feng, D. Du, Y. Lin, *ACS Energy Lett.* **2018**, *3*, 1713.
- [3] S. Cobo, J. Heidkamp, P.-A. Jacques, J. Fize, V. Fourmond, L. Guetaz, B. Jousseme, V. Ivanova, H. Dau, S. Palacin, M. Fontecave, V. Artero, *Nat. Mater.* **2012**, *11*, 802.
- [4] S. Haschke, M. Mader, S. Schlicht, A. M. Roberts, A. M. Angeles-Boza, J. A. C. Barth, J. Bachmann, *Nat. Commun.* **2018**, *9*, 4565.



- [5] W. Yang, Z. Wang, W. Zhang, S. Guo, *Trends Chem.* **2019**, *1*, 259.
- [6] J. Song, C. Wei, Z.-F. Huang, C. Liu, L. Zeng, X. Wang, Z. J. Xu, *Chem. Soc. Rev.* **2020**, *49*, 2196.
- [7] F. Yang, T. Xiong, P. Huang, S. Zhou, Q. Tan, H. Yang, Y. Huang, M.-S. (J. T.) Balogun, *Chem. Eng. J.* **2021**, *423*, 130279.
- [8] W. Cheng, X. Zhao, H. Su, F. Tang, W. Che, H. Zhang, Q. Liu, *Nat. Energy* **2019**, *4*, 115.
- [9] X. Niu, Q. Shi, W. Zhu, D. Liu, H. Tian, S. Fu, N. Cheng, S. Li, J. N. Smith, D. Du, Y. Lin, *Biosens. Bioelectron.* **2019**, *142*, 111495.
- [10] H. Tian, W. Zhu, Q. Shi, S. Ding, Z. Lyu, M. Xu, X. Pan, M. H. Engelhard, D. Dan, Y. Lin, *J. Mater. Chem. A* **2022**, *10*, 11196.
- [11] T. Reier, M. Oezaslan, P. Strasser, *ACS Catal.* **2012**, *2*, 1765.
- [12] V. Pfeifer, T. E. Jones, S. Wrabetz, C. Massué, J. J. Velasco Vélez, R. Arrigo, M. Scherzer, S. Piccinin, M. Hävecker, A. Knop-Gericke, R. Schlögl, *Chem. Sci.* **2016**, *7*, 6791.
- [13] H. Huang, S. Ning, Y. Xie, Z. He, J. Teng, Z. Chen, Y. Fan, J.-Y. Shi, M. Barboiu, D. Wang, C.-Y. Su, *Small* **2023**, *19*, 2302272.
- [14] Y. Huang, F. Pei, G. Ma, Z. Ye, X. Peng, D. Li, Z. Jin, *ACS Appl. Mater. Interfaces* **2022**, *14*, 784.
- [15] K. Zhu, X. Zhu, W. Yang, *Angew. Chem., Int. Ed.* **2019**, *58*, 1252.
- [16] L. Hu, R. Xiao, D. Du, C. Zhu, Y. Lin, *Trends Chem.* **2023**, *5*, 324.
- [17] S. Ding, L. He, L. Fang, Y. Zhu, T. Li, Z. Lyu, D. Du, Y. Lin, J.-C. Li, *Adv. Energy Mater.* **2022**, *12*, 2202984.
- [18] J. Zhao, J.-J. Zhang, Z.-Y. Li, X.-H. Bu, *Small* **2020**, *16*, 2003916.
- [19] S. Anantharaj, S. Kundu, S. Noda, *Nano Energy* **2021**, *80*, 105514.
- [20] L. Hu, R. Xiao, X. Wang, X. Wang, C. Wang, J. Wen, W. Gu, C. Zhu, *Appl. Catal., B* **2021**, *298*, 120599.
- [21] L. Hu, M. Li, X. Wei, H. Wang, Y. Wu, J. Wen, W. Gu, C. Zhu, *Chem. Eng. J.* **2020**, *398*, 125605.
- [22] L. Hu, X. Zeng, X. Wei, H. Wang, Y. Wu, W. Gu, L. Shi, C. Zhu, *Appl. Catal., B* **2020**, *273*, 119014.
- [23] P. W. Menezes, A. Indra, C. Das, C. Walter, C. Göbel, V. Gutkin, D. Schmei?Er, M. Driess, *ACS Catal.* **2017**, *7*, 103.
- [24] K. Gao, B. Wang, L. Tao, B. V. Cunnings, Z. Zhang, S. Wang, R. S. Ruoff, L. Qu, *Adv. Mater.* **2019**, *31*, 1805121.
- [25] T. Xiong, X. Yao, Z. Zhu, R. Xiao, Y.-W. Hu, Y. Huang, S. Zhang, M.-S. (J. T.) Balogun, *Small* **2022**, *18*, 2105331.
- [26] B. Hao, Z. Ye, J. Xu, L. Li, J. Huang, X. Peng, D. Li, Z. Jin, G. Ma, *Chem. Eng. J.* **2021**, *410*, 128340.
- [27] Y. Feng, H. Zhang, L. Fang, Y. Mu, Y. Wang, *ACS Catal.* **2016**, *6*, 4477.
- [28] Z. Zhang, Y. Qin, M. Dou, J. Ji, F. Wang, *Nano Energy* **2016**, *30*, 426.
- [29] D. Liu, J.-C. Li, S. Ding, Z. Lyu, S. Feng, H. Tian, C. Huyan, M. Xu, T. Li, D. Du, P. Liu, M. Shao, Y. Lin, *Small Methods* **2020**, *4*, 1900827.
- [30] Z. Lyu, S. Ding, D. Du, K. Qiu, J. Liu, K. Hayashi, X. Zhang, Y. Lin, *Adv. Drug Delivery Rev.* **2022**, *185*, 114269.
- [31] X. Yang, K. Li, G. Wang, X. Li, P. Zhou, S. Ding, Z. Lyu, Y.-C. Chang, Y. Zhou, W. Zhu, *Chem. Eur. J.* **2022**, *28*, e202201881.
- [32] S. Fu, J. Song, C. Zhu, G.-L. Xu, K. Amine, C. Sun, X. Li, M. H. Engelhard, D. Du, Y. Lin, *Nano Energy* **2018**, *44*, 319.
- [33] P. Su, W. Pei, X. Wang, Y. Ma, Q. Jiang, J. Liang, S. Zhou, J. Zhao, J. Liu, G. Q. (M.) Lu, *Angew. Chem.* **2021**, *133*, 16180.
- [34] H. Liu, X. Lu, Y. Hu, R. Chen, P. Zhao, L. Wang, G. Zhu, L. Ma, Z. Jin, *J. Mater. Chem. A* **2019**, *7*, 12489.
- [35] M. Jahan, Z. Liu, K. P. Loh, *Adv. Funct. Mater.* **2013**, *23*, 5363.
- [36] B. Ali, S. Tasirin, P. Aminayi, Z. Yaakob, N. Ali, W. Noori, *Nanomaterials* **2018**, *8*, 1053.
- [37] J. R. do Nascimento, M. R. D'Oliveira, A. G. Veiga, C. A. Chagas, M. Schmal, *ACS Omega* **2020**, *5*, 25568.
- [38] K. Wang, J. Guo, H. Zhang, *Mater. Adv.* **2022**, *3*, 6887.
- [39] M. Wang, Z. Feng, *Chem. Commun.* **2021**, *57*, 10453.
- [40] M. Wang, Z. Feng, *Current Opinion in Electrochemistry* **2021**, *30*, 100803.
- [41] M. Wang, L. Árnadóttir, Z. J. Xu, Z. Feng, *Nano-Micro Lett.* **2019**, *11*, 47.
- [42] Y.-N. Gong, L. Jiao, Y. Qian, C.-Y. Pan, L. Zheng, X. Cai, B. Liu, S.-H. Yu, H.-L. Jiang, *Angew. Chem.* **2020**, *132*, 2727.
- [43] X. Zhang, Y. Li, Z. Wu, H. Sheng, Y. Hu, C. Li, H. Li, L. Cao, B. Dong, *Mater. Today Energy* **2022**, *26*, 100987.
- [44] X. Li, P. F. Liu, L. Zhang, M. Y. Zu, Y. X. Yang, H. G. Yang, *Chem. Commun.* **2016**, *52*, 10566.
- [45] B. You, N. Jiang, M. Sheng, M. W. Bhushan, Y. Sun, *ACS Catal.* **2016**, *6*, 714.
- [46] Y. Feng, X.-Y. Yu, U. Paik, *Sci. Rep.* **2016**, *6*, 1.
- [47] X. Cui, P. Ren, D. Deng, J. Deng, X. Bao, *Energy Environ. Sci.* **2016**, *9*, 123.
- [48] K. Ruan, Y. Guo, C. Lu, X. Shi, T. Ma, Y. Zhang, J. Kong, J. Gu, *Research* **2021**, *54*, 4934.
- [49] S. Ding, Z. Lyu, E. Sarnello, M. Xu, L. Fang, H. Tian, S. E. Karcher, T. Li, X. Pan, J. McCloy, G. Ding, Q. Zhang, Q. Shi, D. Du, J.-C. Li, X. Zhang, Y. Lin, *J. Mater. Chem. A* **2022**, *10*, 5981.
- [50] G. Bharath, B. S. Latha, E. H. Alsharaeh, P. Prakash, N. Ponpandian, *Anal. Methods* **2017**, *9*, 240.
- [51] S. Ding, Z. Lyu, L. Fang, T. Li, W. Zhu, S. Li, X. Li, J.-C. Li, D. Du, Y. Lin, *Small* **2021**, *17*, 2100664.
- [52] S. Ding, J. A. Barr, Q. Shi, Y. Zeng, P. Tieu, Z. Lyu, L. Fang, T. Li, X. Pan, S. P. Beckman, D. Du, H. Lin, J.-C. Li, G. Wu, Y. Lin, *ACS Nano* **2022**, *16*, 15165.
- [53] J.-C. Li, F. Xiao, H. Zhong, T. Li, M. Xu, L. Ma, M. Cheng, D. Liu, S. Feng, Q. Shi, H.-M. Cheng, C. Liu, D. Du, S. P. Beckman, X. Pan, Y. Lin, M. Shao, *ACS Catal.* **2019**, *9*, 5929.
- [54] G.-F. Chen, T. Y. Ma, Z.-Q. Liu, N. Li, Y.-Z. Su, K. Davey, S.-Z. Qiao, *Adv. Funct. Mater.* **2016**, *26*, 3314.
- [55] Y. Jin, H. Wang, J. Li, X. Yue, Y. Han, P. K. Shen, Y. Cui, *Adv. Mater.* **2016**, *28*, 3785.
- [56] Y. Tu, P. Ren, D. Deng, X. Bao, *Nano Energy* **2018**, *52*, 494.
- [57] K. Xu, H. Cheng, L. Liu, H. Lv, X. Wu, C. Wu, Y. Xie, *Nano Lett.* **2017**, *17*, 578.
- [58] B. Zhang, Y. H. Lui, H. Ni, S. Hu, *Nano Energy* **2017**, *38*, 553.
- [59] P. Wei, X. Sun, Q. Liang, X. Li, Z. He, X. Hu, J. Zhang, M. Wang, Q. Li, H. Yang, J. Han, Y. Huang, *ACS Appl. Mater. Interfaces* **2020**, *12*, 31503.
- [60] M. Görlin, P. Chernev, J. Ferreira De Araújo, T. Reier, S. Dresch, B. Paul, R. Krähnert, H. Dau, P. Strasser, *J. Am. Chem. Soc.* **2016**, *138*, 5603.